

DEFORMATION BANDS ON MARS AND IMPLICATIONS FOR SUBSURFACE FLUID FLOW. C.H. Okubo, and The HiRISE Team, Lunar and Planetary Laboratory, University of Arizona, Tucson, AZ, 85721 (chriso@lpl.arizona.edu)

Introduction: Clastic sedimentary deposits are well-known source regions for terrestrial underground reservoirs of volatiles because of the high porosities and permeabilities of these rocks [1,2]. Faults and their surrounding damage zones play an important role in controlling the pathways along which volatiles tend to migrate within these reservoirs. This is because faults and attendant damage zones can act as either barriers [3–6] or conduits [7–9] to the movement of volatiles within the reservoir. Where exposed through erosion, fault-controlled reservoirs offer excellent opportunities to examine past tectonic, geochemical, hydrologic and biologic processes that originally occurred in the subsurface.

The light-toned layered deposits on Mars show abundant evidence of diagenetic alteration that is attributed to subsurface fluid flow. These deposits are in places highly fractured. Therefore understanding the implications of brittle fracturing on fluid flow potential through these deposits is a key to interpreting the geologic history of water and other volatiles. Accordingly on Mars, faulted sedimentary deposits that have been exhumed through erosion are logical places to look for evidence of past or present volatile-related processes.

Faults exhumed by erosion are commonly observed within the layered deposits and are expressed as linear discontinuities along which bedding is offset [10–12]. Recent images from the High Resolution Imaging Science Experiment (HiRISE) [13] provide highly-detailed views of the damage zones that surround faults in the layered deposits and enable more in depth studies of the fluid flow implications of these faults.

A fault related damage zone on Mars: Erosional exposures through a mound of layered deposits that partially fill a *ca.* 63 km diameter impact crater in Arabia Terra (Fig. 1) provide an clear example of a fault-related damage zone. Within the surrounding crater floor, thrust fault-related folds (known morphologically as ‘wrinkle ridges’ [14,15]) are present. The sinuous topography of these folds extends onto the mound of layered deposits, suggesting that the layered deposits within the mound have been folded as well.

Figure 2 shows an erosional surface through the mound of layered deposits within a north–south trending fold. This exposure provides a window into the fold’s internal thrust fault and damage zone structure. The damage zone is manifest as a zone of inosculating ridges that have a positive relief. These ridges are up to *ca.* 2–3 m wide. Meter-scale offsets of sedimentary layers across these ridges are also present. Individual ridges are interpreted to be a cluster of many closely-spaced sub-parallel deformation bands.

Deformation bands are tabular structures that accommodate shear and normal strain through localized changes in

porosity and grain size [16–20]. During brittle deformation, porosity within the band may increase or decrease depending on the initial porosity and applied stresses [17–20]. These changes in host rock porosity affect permeability [19,20]. Single deformation bands and clusters of deformation bands commonly constitute terrestrial damage zones in porous sedimentary rock (Figs. 3,4).

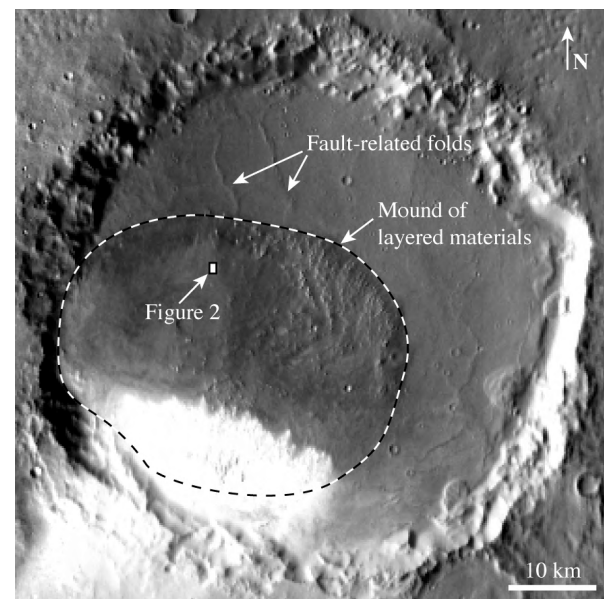


Figure 1. Location of the study area. This crater is centered at 14.29 E, 6.57 N (IAU 2000; planetocentric). Illumination from the right. THEMIS VIS mosaic.

Deformation bands are precursors to, and form contemporaneously with, faults in porous and granular rocks and soils [4,5,16–18]. A few of the thicker clusters of deformation bands may contain fault slip surfaces. Clusters of deformation bands on Earth (Fig. 4) typically increase in thickness through the initiation and propagation of new parallel bands [4,5,16]. The thickness of the deformation band cluster increases until strain hardening is sufficiently large to promote the initiation and propagation of fault patches [17,18].

Mechanics of faulting in granular geomaterials: The onset of brittle deformation in granular rocks and soils is commonly described by a capped yield envelope (Fig. 5) in the domain of stress invariants Q , differential stress, $Q = \sigma_1 - \sigma_3$, and P , effective mean stress, $P = [(\sigma_1 + 2\sigma_3)/3] - P_i$, where P_i is pore pressure [e.g., 19,20]. This yield envelope defines the critical stress states at which elastic strain changes to irrecoverable, plastic strain.

The yield envelopes (i.e. the maximum strengths) for granular rocks (Fig. 5) are a direct function of grain size and porosity [19,20]. Laboratory testing has shown that yield envelopes for granular rocks can be described by the equation

$$\text{Eq. 1} \quad \frac{(P/P^* - \delta)^2}{(1 - \delta)^2} + \frac{(Q/P^*)^2}{\gamma^2} = 1 \quad [1]$$

[19,20]. Here, δ and γ are unitless empirical coefficients. Laboratory testing has shown that $\delta \approx 0.5$ and values of γ range between 0.5 and 0.7 for a variety of sedimentary rocks [19,20]. Also in equation 1, P^* is the grain crushing pressure. Values of $\delta = 0.5$ and $\gamma = 0.6$ are used here.

Values of P^* can be determined experimentally or from empirical relationships of grain size, porosity or both [19,20]. Values of P^* have been established for the light-toned layered deposits examined by MER Opportunity using measurements of apparent porosity [21]. Calculated values of P^* , for the layered deposits examined between Eagle Crater and Erebus Crater, have a median value of 6.9 MPa under drained (dry) groundwater conditions.

The strength envelope for the layered deposits is calculated from the median value of P^* and equation 1 (Fig. 2). The magnitude of P^* for the water saturated strength envelope is reduced by 50% to 3.5 MPa, in line with results of laboratory tests on terrestrial sedimentary rock [19,20].

In granular rocks, compaction and dilation are largely achieved through volumetric strain of pore space. These changes in inter-granular pore volume are accommodated through reordering of grain packing geometry via grain translation and rotation, which is facilitated by bulk shear displacements for non-trivial magnitudes of Q . The type of fracture that forms in these materials varies systematically along the strength envelope (Fig. 5) [17–22].

Where Q is zero and P is near-minimum for brittle deformation, ‘dilation bands’ occur through increases in pore space (with zero shear displacement) localized along a tabular discontinuity. At increasing magnitudes of P and Q , brittle deformation occurs by decreasing magnitudes of pore space dilation with increasing magnitudes of shear along a band. Deformation in this region occurs through localized shear-enhanced dilation, which drives the growth of ‘dilation deformation bands’.

The strength function peaks at a maximum Q value, Q_{\max} , which serves to delineate the ‘dilational side’ of the yield envelope at lower magnitudes of P from the ‘compactional side’ at higher magnitudes of P . Past Q_{\max} , with increasing P and decreasing Q , brittle deformation occurs by increasing magnitudes of pore space compaction with decreasing magnitudes of shear along a band. On the immediate compactional side of Q_{\max} , shear-enhanced compaction drives the growth of ‘compactional deformation bands’.

the maximum value of P along the envelope, compaction (with zero shear) localizes along ‘compaction bands’.

Brittle deformation that occurs through the formation of dilation bands and dilational deformation bands is accompanied by increases in porosity and permeability, while decreases in porosity and permeability accompany the development of compaction bands and compactional deformation bands [17–20,23–25]. Thus dilation bands and dilational deformation bands enhance fluid flow, while compaction bands and compactional deformation bands generally form barriers to fluid flow.

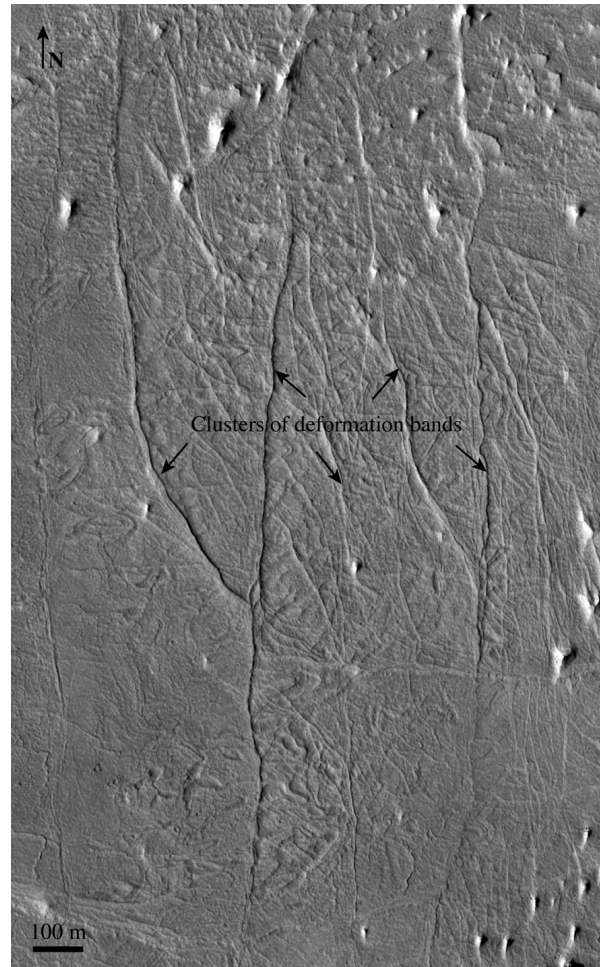


Figure 2. Deformation band damage zones within a thrust fault-related fold. Illumination from the right. HiRISE image PSP_002574_1865.

Discussion: A first order determination of the types of deformation bands that are observed in figure 2, and their fluid flow implications, can be made with currently available data. To do this, location where the causative loading path in Q,P space crosses the strength envelope must be determined. The point at which the loading path crosses the strength envelope determines the type of band that will form. The load-

ing path is first estimated for two end members, 1) an increasing lithostatic load due to accumulation of overburden (layered deposits), and 2) increasing driving stresses for thrust faulting.

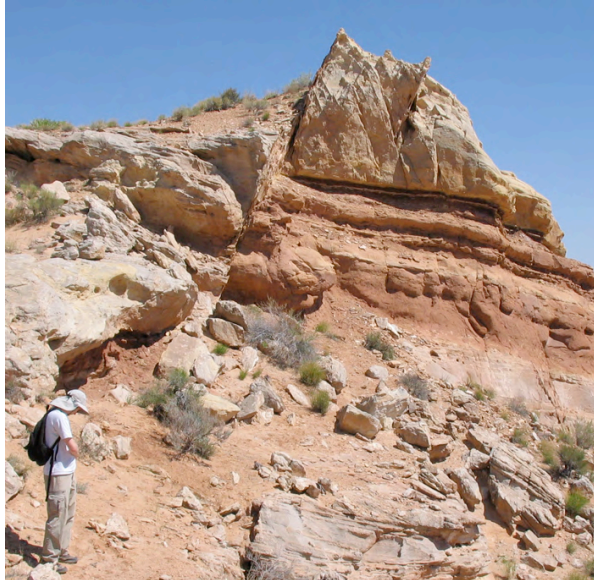


Figure 3. Clusters of deformation bands and individual bands within a fault-related damage zone. This fault has a normal sense of slip. This outcrop is located at UTM 12 525793E 4271343N (NAD27) and is described in detail by [26].

The load path for increasing lithostatic load alone (first end member) is simply, $\sigma_1 = \rho g z$ and $\sigma_3 = \nu \sigma_1$, where σ_1 is lithostatic load, σ_3 is the least compressive horizontal principal stress, ρ is density (2200 kg/m^3), g is gravitational acceleration (3.71 m/s^2), z is depth and ν is Poisson's ratio (0.25). Values for ρ and ν are based on typical values for terrestrial sandstones [27].

The lithostatic load path is calculated up to a depth of 1 km, based on the thicknesses of layered deposits in adjacent craters. The mound of layered deposits shown in figure 1 has a maximum elevation of *ca.* -1380 m. Adjacent craters of similar diameter (at 11.80 E, 6.67 N and 10.14 E, 6.95 N, planetocentric) have mounds of layered deposits that reach an elevation of *ca.* -450 m. If this crater were filled by layered deposits to this common elevation, the area of figure 1 would have been buried at a depth of at least *ca.* 960 m. Based on these considerations, lithostatic load paths are shown on figure 5 for both wet and dry groundwater conditions.

The load path corresponding to increasing driving stresses for thrust faulting (second end member) is calculated using the Coulomb failure criterion in principal stress form,

$$\text{Eq. 2} \quad \sigma_1 = \sigma_c + \sigma_3 \left(\sqrt{\mu^2 + 1} + \mu \right)^2 \quad [28]$$

where σ_1 is the most compressive horizontal principal stress and σ_3 is lithostatic load, as consistent with the Andersonian stress state for thrust faulting [29]. The parameter σ_c is the unconfined compressive strength of the geomaterial and μ is its friction coefficient. A median value for σ_c of 8.9 MPa under drained groundwater conditions is calculated for the layered deposits examined by Opportunity [21]. Measured values of μ typically range between 0.2 and 0.85 [27]. A median value for μ of 0.53 is used here.

The transition in loading paths from purely lithostatic loading to thrust faulting requires a change in the orientation of the most compressive stress, σ_1 . In the increasing lithostatic load case, σ_1 is vertical and σ_3 is horizontal. In the stress state for thrust faulting however, σ_1 is horizontal and σ_3 is vertical [29]. Therefore the magnitude of the horizontal stress must approach, then exceed the magnitude of the vertical stress. In doing so, the differential stress (Q) will go to zero. The magnitude of Q will then increase with increasing (horizontal) σ_1 . The magnitude of P will increase throughout assuming negligible erosion. The magnitude of σ_1 would then increase until the Coulomb conditions for thrust faulting are met. An example of this loading scenario is shown in figure 5.



Figure 4. A narrow cluster of deformation bands. The thin white lineations are individual compactional deformation bands. Same locality as figure 3.

A variety of band types are predicted to form through this 'transitional' loading scenario. During lithostatic loading, dilation bands would form as the load path crosses the dilational side of the strength envelope. This is predicted for both the dry (red circle in figure 5B) and wet conditions at overburden depths of *ca.* 800 m and 400 m respectively. Increasing horizontal stress due to tectonic compression causes Q to drop to zero, and increases P , resulting in compactional deformation band formation (red stars in figure 5B) followed by compaction band formation if $P > P^*$ (red diamond in figure 5B). Finally, with increasing magnitudes of Q and P , compactional deformation bands form. These bands

form damage zones that are precursors to thrust faults. Magnitudes of Q and P continue to increase until the Coulomb criterion for faulting is met, at which point thrust faults begin to form contemporaneously with compactional deformation bands within the surrounding damage zone. Structures that are morphologically consistent with dilational and compactional deformation bands, as well as compaction bands, are indeed observed in figure 2.

This scenario would result in sets of crosscutting bands and have significant implications for fluid flow. The initial dilational deformation bands will enhance fluid flow along the plane of the bands (fracture-supported flow). Fluid flow will be impeded across subsequent compactional deformation bands and compaction bands, resulting in matrix-supported flow that is channelized parallel to the bands.

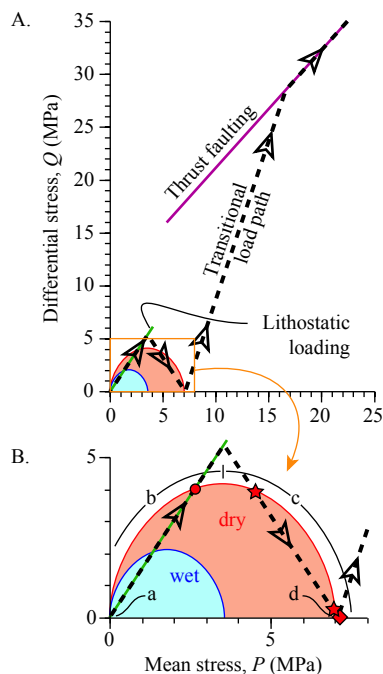


Figure 5. Strength envelopes for light-toned layered deposits under dry (red curve) and wet (blue curve) ground water conditions. An expanded view of the area in the orange box in A is shown in B. Stress states that fall below the strength envelope (e.g. red-shaded area for the dry curve) result in elastic deformation. Brittle deformation occurs where the loading path crosses the strength envelope (e.g. red circle and stars along the transitional load path). Types of bands that form along the strength envelope are labeled (a) dilation bands, (b) dilational deformation bands, (c) Compactional deformation bands, (d) compaction bands.

Understanding the orientations of these bands is important for predicting specific patterns of paleo-fluid flow. The orientation and frequency distributions of bands is dependent on the loading path that the geomaterials follow from initial

lithostatic loading to thrust faulting. Additionally, changes in host rock porosity due to this deformation will cause variations in the size of the strength envelope in Q,P space. Local stresses around bands and faults, not discussed here, will also influence the types of bands that subsequently form.

Such time-dependent three-dimensional geometries of fault-related damage zones can be predicted using numerical models of fault geometry, driving stress, and values of material strength and deformability [22,30]. These analyses will provide insight into fault-controlled fluid flow. These aspects are important in evaluating the growth and productivity of structurally-controlled fluid reservoirs within the layered deposits. This future work will also help to identify areas of past fluid flow, and potential past habitable oases, for further investigation with orbiter and lander based instruments.

References: [1] Coward M.P. et al. (1998) *Structural geology in reservoir characterization*. Geol. Soc. London, Spec. Pub. 127, 290 pp. [2] Haneberg W.C. et al. (1999) *Faults and Subsurface Fluid Flow in the Shallow Crust*. AGU, Geophys. Mon. 113, 222 pp. [3] Jamison W.R. and Stearns D.W. (1982) *AAPG Bull.*, 66, 2584–2608. [4] Antonellini M. and Aydin A. (1994) *AAPG Bull.*, 78, 355–377. [5] Shipton Z.K. et al. (2002) *AAPG Bull.*, 86, 863–883. [6] Sigda J.M. and Wilson J.L. (2003) *Water Resources Res.*, 39, 1225. [7] Sibson R.H. (1996) *J. Struct. Geol.*, 18, 1031–1042. [8] Campbell K. et al. (2003) *J. Contam. Geol.*, 62–63, 143–161. [9] Tripp G.I. and Vearncombe J.R. (2004) *J. Struct. Geol.*, 26, 1087–1108. [10] Malin M.C. and Edgett K.S. (2000) *Science*, 290, 1927–1937. [11] Edgett K.S. (2002) *JGR*, 107, 5038. [12] Weitz K.M. et al., (2007) *LPS XXXVIII*, Abstract #1442. [13] McEwen A.S. et al. (2007) *JGR*, in press. [14] Schultz R.A. (2000) *JGR*, 105, 12035–12052. [15] Okubo C.H. and Schultz R.A. (2004) *GSA Bull.*, 116, 594–605. [16] Aydin A. and Johnson A. (1978) *Pure Appl. Geophys.*, 116, 931–942. [17] Schultz R.A. and Sidharthan R. (2005) *Tectonophysics*, 411, 1–18. [18] Aydin A. et al. (2006) *J. Struct. Geol.*, 28, 83–98. [19] Wong T.-f. et al. (2004) in *Mechanics of Fluid Saturated Rocks*, Academic Press, 55–114. [20] Wong T.-f. et al. (1997) *JGR*, 102, 3009–3025. [21] Okubo C.H. et al. (2007) abstract submitted to 7th Int. Conf. Mars (this volume). [22] Okubo C.H. and Schultz R.A. (2006) *J. Geol. Soc.*, 162, 939–950. [23] Zhu W. and Wong T.-f. (1997) *JGR*, 102, 3027–3041. [24] Zhu W. et al. (1997) *Mech. Mat.*, 25, 199–214. [25] Vajdova V.P. et al. (2004) *JGR*, 109, B10406 [26] Schultz R.A. and Fossen H. (2002) *J. Struct. Geol.*, 24, 1389–1411. [27] Lama R.D. and Vutukuri V.S (1978) *Handbook on Mechanical Properties of Rocks*, v. 2, Trans Tech Publications, 481 pp. [28] Goodman R.E. (1989) *Introduction to Rock Mechanics*, John Wiley & Sons, 562 pp. [29] Anderson E.M. (1951) *The dynamics of faulting and dyke formation, with applications to Britain*, Oliver & Boyd, 260 pp. [30] Okubo C.H. and Schultz R.A. (2006) *GSA Bull.*, 118, 343–348.

Acknowledgements: This work is supported by a grant from NASA's Mars Data Analysis Program to C. Okubo (05-MDAP05-0002). HiRISE data from <http://hirise.lpl.arizona.edu>.